Ultrafine Nickel Nanoparticles Encapsulated in N-Doped Carbon Promoting Hydrogen Oxidation Reaction in Alkaline Media

Jie Wang,[∥] Xue Dong,[∥] Jing Liu,* Wenzhen Li, Luke T. Roling, Jianping Xiao,* and Luhua Jiang*

ACCESS | 📊 Metrics & More | 📖 Article Recommendations | 🆚 Supporting Information

ABSTRACT: Developing low-cost and robust hydrogen oxidation reaction (HOR) electrocatalysts is urgent for anion exchange membrane fuel cells (AEMFCs). Herein, we report an efficient Ni-based catalyst for HOR in alkaline electrolyte, which features an ultrafine Ni nanoparticle (3.7 nm) core and an ultrathin N-doped carbon shell (0.36 nm). The optimized catalyst exhibits both excellent activity (24.4 A g^{-1}_{Ni} @ η = 50 mV and exchange current density of 38 μA cm^{-2}_{Ni}) and superior stability for the HOR. Theoretical calculations reveal that the d-band state of Ni encapsulated in ultrathin N-doped carbon shell is downshifted, with optimal binding energies of OH_{ad} and H_{ad}, leading to a low limiting energy pathway for HOR.

KEYWORDS: *hydrogen oxidation reaction, anion exchange membrane fuel cell, Ni nanoparticles, encapsulating, electrocatalyst*
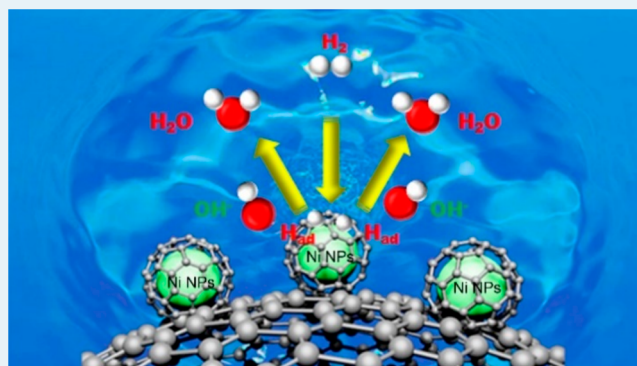
Anion exchange membrane fuel cells (AEMFCs) have attracted increasing attention, owing to their potential to utilize nonplatinum group metal (NPGM) electrocatalysts and thus reduce the cost of fuel cells.[1−3] Although the hydrogen oxidation reaction (HOR) is quite fast in acidic media over Pt, it is kinetically 2 orders of magnitude slower in alkaline media, which becomes the bottleneck for the development of AEMFCs.[4−8] Therefore, it is urgent to develop low-cost yet highly efficient and stable HOR electrocatalysts in alkaline media.

For the HOR process in alkaline media, an H_2 molecule first dissociates with the formation of surface H_{ad} via either a Tafel step (H_2 + 2 M ⇌ 2M-H_{ad}) or a Heyrovsky step (H_2 + OH^- + M ⇌ M-H_{ad} + H_2O + e^-) and then undergoes a Volmer step (M-H_{ad} + OH^- ⇌ H_2O + e- + M).[9,10] On the basis of the Sabatier principle, a moderate binding energy of reaction intermediates over catalyst surfaces (i.e., hydrogen binding energy (HBE) and hydroxide binding energy (OHBE)) is preferred to achieve a high activity.[11−17] Ni-based catalysts have attracted plenty of interest because of a reasonable HOR activity and abundant resources on earth. However, the Ni surface is known to be too active for both hydrogen and oxygen, so the strong binding with H_{ad} and OH_{ad} results in considerable activity disparity between the state-of-the-art Ni catalyst and the commercial Pt benchmark, and poor stability associated with surface passivation. To suppress the strong interaction of the 3d orbital of Ni with the intermediates (i.e., H_{ad}, OH_{ad}), some strategies, such as alloying, nitriding, heterostructured design, and strain engineering, have been proposed.[18−25] Recently, it has been reported that HBE over

Ni surface could be modulated by tuning the d band states of Ni via manipulating the Ni−support interaction.[26−28] Yan's group demonstrated that Ni nanoparticles (NPs) supported on N-doped carbon nanotubes are highly active for the HOR in alkaline media.[29] Furthermore, first-principles calculations confirmed the enhanced interaction between metal and heteroatom-doping graphene leads to downshift of the d band center of Ni and thus weakened adsorption of intermediates, and it was consequently predicted that the interfacial sites of Ni/N-graphene were most active for HOR.[30] According to these findings, presumably there is a great chance to obtain highly active Ni catalysts with modulated d band states by minimizing Ni particle size, taking advantage of abundant interfacial active sites and optimized electronic structure.

To address the stability issue of the Ni catalyst, encapsulation of transition metal NPs into a protected shell is considered a promising approach. Gao et al. reported that hexagonal boron nitride (h-BN) shell encapsulated Ni NPs displayed more promising HOR catalytic activity and stability than pure Ni.[26] The Zhuang group also demonstrated improved antioxidation capability of Ni particles (16 nm) in
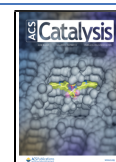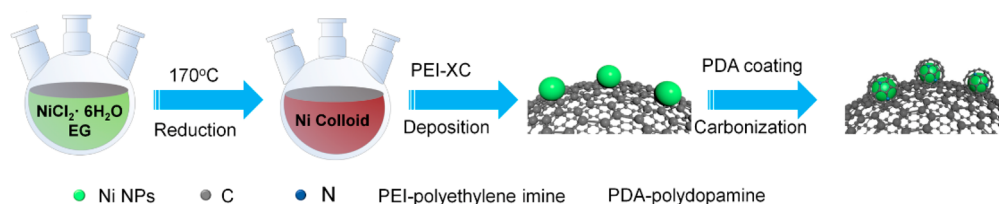
Figure 1. Illustration of preparation route for Ni@NC/PEI-XC.

a Ni-carbon composite with a core−shell structure.[31] Taken together, integrating ultrafine and highly uniform Ni NPs encapsulated in a N-doped carbon shell is reasonably expected to deliver favorable HOR catalytic behavior. However, most of the traditional encapsulated metal catalysts are synthesized by mixing transitional metal precursors and carbon sources together, followed by a thermal treatment.[32,33] These approaches could not simultaneously control the metal particle size and the carbon shell thickness. To the best of our knowledge, ultrafine Ni NPs smaller than 5 nm encapsulated in ultrathin heteroatom-doped carbon have never been synthesized for electrocatalyzing HOR. Herein, we fabricate a unique core−shell structured Ni catalyst with ultrafine Ni NPs (3.7 nm) as the core and N-doped carbon as the shell (denoted as Ni@NC/PEI-XC). Such a distinctive structure enables both a large specific surface area and moderate HBE and OHBE, leading to a high HOR activity. Moreover, the ultrathin heteroatom-doped carbon shell protects the metallic Ni against oxidation, resulting in satisfactory stability.

The preparation route for the Ni@NC/PEI-XC catalyst is illustrated in Figure 1. First, colloidal Ni particles were synthesized by a modified polyol method referred to previous works.[20,34] To obtain well-dispersed Ni NPs on the carbon support, carbon black (Vulcan XC72, abbreviated as XC) was modified previously by polyethylenimine (PEI), which is a cationic polymer with abundant amino groups. After depositing Ni NPs on the PEI modified XC (PEI-XC), the sample experienced a polydopamine (PDA) coating process, followed by a thermal treatment, to obtain the Ni@NC/PEI-XC catalyst. For comparison, Ni/XC (without PEI modification and PDA coating) and Ni/PEI-XC (without PDA coating) were also synthesized (see the Experimental Section in the Supporting Information for details).

The Ni particles in both Ni@NC/PEI-XC and Ni/PEI-XC distributed uniformly on the carbon support, as displayed in the TEM images in Figure 2a and Figure S1a, benefiting from the abundant amino groups in PEI, which can anchor metals. In contrast, Ni NPs in Ni/XC (Figure S1b) show obvious agglomeration with a larger particle size of 7.2 nm. The particles in Ni@NC/PEI-XC with a coating time of 15 min are as small as 3.7 nm on average, and a further high-resolution TEM (HRTEM) image (Figure 2b) clearly exhibits a Ni-core/ carbon-shell structured particle. The carbon shell is about 0.36 nm, and the core is metallic Ni based on the interplanar spacing of 0.20 nm corresponding to Ni (111) planes (Figure 2c). The core−shell structure is more obvious for Ni@NC/ PEI-XC-30 min and Ni@NC/PEI-XC-60 min, as shown in panels d and e, respectively, of Figure 2, with an increase in thickness of the carbon shells to 1.00 and 1.43 nm, together with a larger average particle size (4.8 and 5.0 nm). If the PDA coating time is shortened to 5 min, the core−shell structure is indistinguishable (Figure S2). Hence, it shows clearly that the thickness of the carbon shell could be controlled by varying the
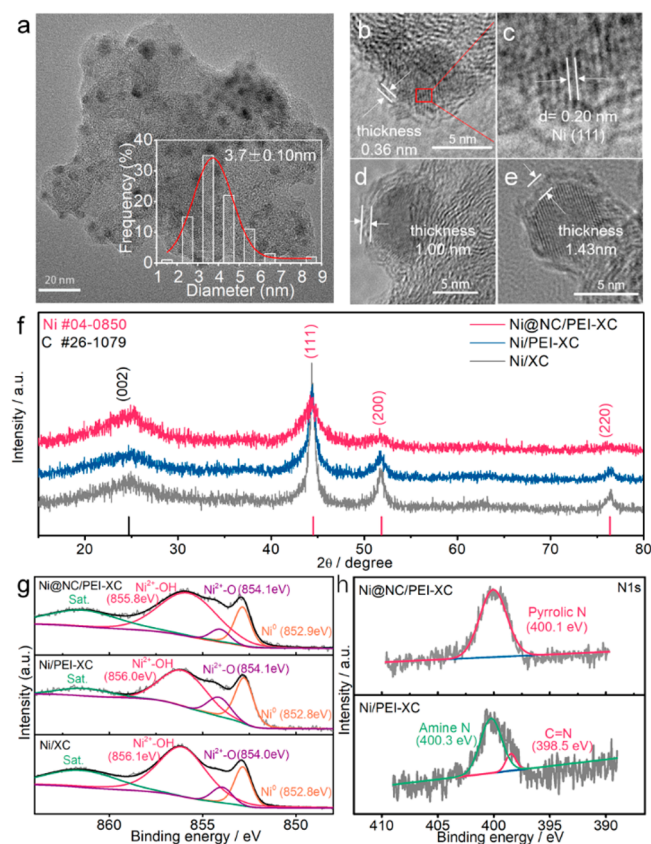

Figure 2. (a) TEM image of Ni@NC/PEI-XC. The inset is the histogram distribution of particle size. (b) HRTEM image of a single particle in Ni@NC/PEI-XC. (c) Enlarged view of the selected area of (b). (d) HRTEM image of a single particle in Ni@NC/PEI-XC-30 min (e) HRTEM image of a single particle in Ni@NC/PEI-XC-60 min (f) XRD patterns of Ni@NC/PEI-XC, Ni/PEI-XC, and Ni/XC catalysts (g) High-resolution Ni 2p XPS spectra of Ni@NC/PEI-XC, Ni/PEI-XC, and Ni/XC. (h) High-resolution N 1s XPS spectrum of Ni@NC/PEI-XC and Ni/PEI-XC.

PDA coating time. The X-ray diffraction patterns (Figure 2f, Figure S3) confirm metallic Ni with a face-centered cubic (fcc) structure (JCPDF#040850) exists in all the Ni-based catalysts, with the diffraction peaks at 44°, 51° and 76° assigned to (111), (200), (220) planes, respectively, and the peak at 25° is assigned to graphitic carbon (JCPDF#261079). Compared with Ni/XC and Ni/PEI-XC, Ni@NC/PEI-XC samples possess much broader diffraction peaks, indicating smaller Ni particles, due to the protection of the PDA coating layers avoiding Ni aggregation during the post thermal-treatment, which is agreeable to the TEM results. The X-ray photo-electron spectrum (XPS) in Figure S4 reveals the coexistence of elements C, N, O, Ni in the Ni@NC/PEI-XC. The high-resolution Ni $2p_{3/2}$ XPS spectrum of Ni@NC/PEI-XC (Figure 2g) could be deconvoluted into four peaks locating at 852.9,

854.1, 855.8, and 861.4 eV, assigned to Ni^0, Ni^{2+} in NiO and Ni$(OH)_2$, and the satellite peaks, respectively. Compared with Ni/XC and Ni/PEI-XC, the Ni^0 peak of Ni@NC/PEI-XC shifts toward higher binding energy by 0.1 eV, indicating a stronger metal−support interaction by electrons transferring from Ni to the support.[19] The presence of Ni^{2+} species in both samples are attributed to Ni oxides that formed inevitably in the air due to surface oxidation. The ratio of Ni^0 to Ni^{2+} on the surface of Ni@NC/PEI-XC is 20.4%, which is similar to that of Ni/XC (19.0%), indicating the similar initial states of Ni species. The high-resolution N 1s spectrum of Ni@NC/PEI-XC displays a peak centered at 400.02 eV (Figure 2h) corresponding to pyrrolic N in the PDA derived carbon shell.[35] Comparatively, Ni/PEI-XC exhibits two peaks located at 398.5 and 400.3 eV, which are attributed to the C=N and amine N species from PEI.[36,37]

The electrocatalytic activities of the Ni-based catalysts for the HOR were evaluated by using a rotating disk electrode (RDE) in H_2-saturated 0.1 M KOH electrolyte. Figure 3a
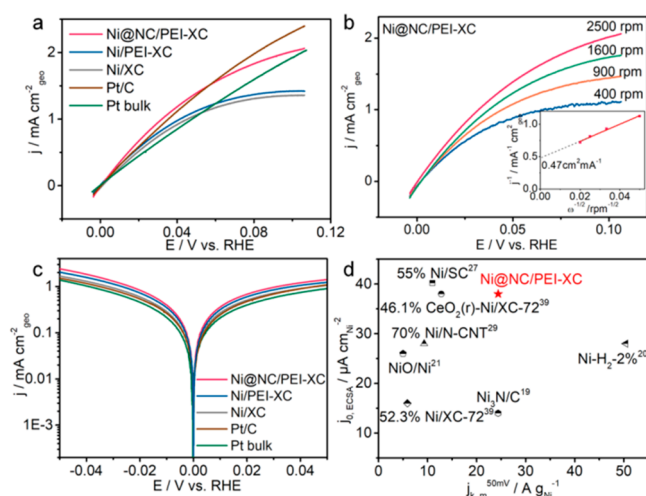
Figure 3. (a) HOR LSV curves of Ni@NC/PEI-XC, Ni/PEI-XC, Ni/XC catalysts, and Pt benchmarks in H_2-saturated 0.1 M KOH at a scan rate of 1 mV s^{-1} and rotation rate of 2500 rpm The loading of the Ni-based catalyst is 255 $\mu g_{cat} cm_{geo}^{-2}$. (b) Polarization curves of Ni@NC/PEI-XC at different rotation rates. Inset is the corresponding Koutecky−Levich plot at 50 mV. (c) The corresponding Tafel plots. (d) Comparison of mass normalized kinetic current densities and specific exchange current densities of Ni@NC/PEI-XC to some reported Ni catalysts.

shows the HOR polarization curves of the Ni-based catalysts. A Pt bulk electrode with a diameter of 5 mm and 20%Pt/C (Johnson Matthey) were used as the benchmark. The Pt loading on the GC electrode was 12.5 $\mu g_{Pt} cm_{geo}^{-2}$. The HOR current density increases following the sequence of Ni/XC < Ni/PEI-XC < Ni@NC/PEI-XC. Ni@NC/PEI-XC exhibits the highest HOR activity, which is superior to that of the Pt bulk electrode (diameter of 5 mm) and competitive with the commercial Pt/C catalyst with low catalyst loading. We note that the different apparent HOR activities between the two benchmark Pt catalysts should be attributed to their differences in Pt surface area (Figure S5). The HOR current density of Ni@NC/PEI-XC increases with the rotation rates (Figure 3b). As shown in the inset of Figure 3b, by fitting the Koutechy− Levich plots (data collected at η = 50 mV), a straight line with a slope of 13.22 cm^2 mA^{-2} rpm$^{1/2}$ could be obtained, which is

in good accordance with the values reported in literature.[38] The kinetic current density (j_k) of the HOR over Ni@NC/ PEI-XC determined from the reciprocal of the y-intercept of the fitting line is 2.12 mA cm$^{-2}_{geo}$. By normalizing the HOR currents to the mass of Ni determined by the inductively coupled plasma-optical emission spectroscopy (ICP-OES) (Table S1), the HOR activity of Ni@NC/PEI-XC is 24.4 A g$^{-1}_{Ni}$, making it among the most active Ni-based electro- catalysts reported to date (Table S2).[19−21,27,29,39] Furthermore, the exchange current densities, which reflect the intrinsic HOR activity, were acquired from the Tafel plots (Figure 3c) according to the Bulter−Volmer equation. Ni@NC/PEI-XC exhibits an exchange current density of 7.84 A g$^{-1}_{Ni}$, which is more than twice that of Ni/XC (Figure S6). Moreover, the electrochemical surface area (ECSA) of the catalysts were estimated from the base CVs of Ni@NC/PEI-XC and Ni/XC (Figure S7) based on the cathodic peak of α-Ni$(OH)_2$ reduction by assuming a monolayer with specific charge of 514 μC cm^{-2}.[40] Ni@NC/PEI-XC exhibits a high ECSA of 20.41 m^{2}g$^{-1}_{Ni}$, as compared with 9.37 m^{2}g$^{-1}_{Ni}$ for Ni/XC, demonstrating abundant active sites exposing, taking advantage of the ultrafine Ni NPs. Even excluding the influence from the ECSA, the j_o of Ni@NC/PEI-XC (38 μA cm$^{-2}_{Ni}$) is also higher than most of the reported Ni-based catalysts for HOR. (Table S2) As shown in Figure 3d, Ni@NC/PEI-XC in this work exhibits superior HOR performance in both mass activity and specific activity. To demonstrate the practical application of the Ni@NC/PEI-XC catalyst, a membrane electrode assembly (MEA) using Ni@NC/PEI-XC as the anode electrocatalyst was fabricated and evaluated. The discharge and power density curves are shown in Figure S8. The H_2−O_2 AEMFC exhibits an open circuit voltage (OCV) of 1.02 V and a peak power density of 241 mW cm^{-2}, which is among the best PGM-free anode based AEMFCs, demonstrating the promising potential application of the Ni@NC/PEI-XC catalyst.[18,31,41]

The carbon shell thickness influences the HOR activity. According to the HOR polarization curves and the Tafel slopes, the ECSA in Figure S9, and the ECSA normalized exchange current density of the Ni@NC/PEI-XC catalysts with different carbon shell thicknesses in Figure S10, it is concluded that thinner carbon shells result in higher HOR activity. The carbon shell thickness as well as particle size, specific activity, and mass activity of HOR on the all the Ni catalysts in this work are summarized in Table S3, showing that as the carbon layer thickness decreases from three to one layer, the intrinsic HOR activity increases by more than 100%. It is reasonable considering the interaction between metal and carbon layers would decline with increasing shell thickness.[33] It should be mentioned that the ultrathin carbon shell of the Ni@ NC/PEI-XC catalyst was derived from the pyrolysis of polydopamine, which is porous and permeable to the reactant gas molecules and ions. To verify this, SCN$^-$, a strong metal- coordination agent, was employed to detect the Ni active sites. The HOR polarization curves were tested in H_2-saturated 0.1 M KOH electrolyte containing 5 mM KSCN on Ni/PEI-XC (without PDA coating), Ni@NC/PEI-XC, and Ni@NC/PEI- XC-60 min catalysts. (Figure S11) All the catalysts exhibit a decreased HOR activity after introducing SCN$^-$ in the electrolyte, demonstrating the critical role of Ni-related active sites. As shown in Figure S12, Ni@NC/PEI-XC retains 29% of the activity in the SCN$^-$ containing electrolyte, which is almost equal to that of Ni/PEI-XC, indicating the efficient SCN$^-$

transport across the ultrathin carbon coating layer. Ni@NC/PEI-XC-60 min with the thickest carbon shell retains 80% of the activity, suggesting that carbon shells might restrict the ion transport if they are too thick. The results suggest that the unique architecture of the core−shell Ni@NC/PEI-XC catalyst is efficient in mass transfer.

To investigate the stability of Ni@NC/PEI-XC catalyst, an accelerated degradation test (ADT) was carried out in H_2-saturated 0.1 M KOH electrolyte by scanning from −4−100 mV_{RHE} for 6000 cycles. The HOR polarization curves on Ni@NC/PEI-XC, Ni/PEI-XC and Ni/XC during the ADT test were recorded (Figure 4a, Figure S13a and S13b). Taking the
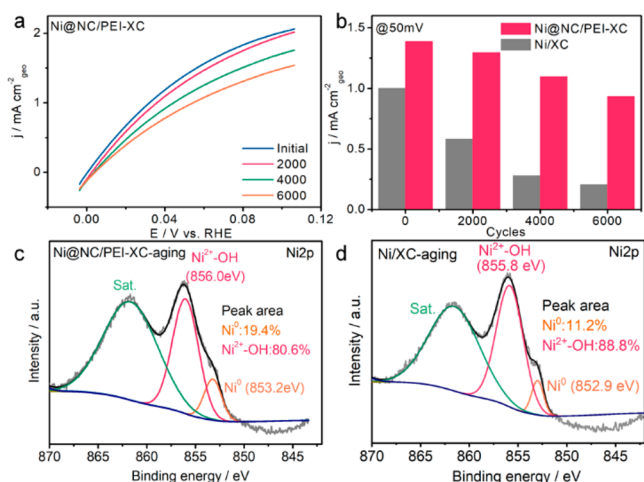

Figure 4. (a) Polarization curves of Ni@NC/PEI-XC during ADT test in H_2-saturated 0.1 M KOH with a scan rate of 1 mV s^{-1} and a rotation rate of 2500 rpm. (b) Current density taken at 50 mV for Ni/XC and Ni@NC/PEI-XC catalyst during the ADT test. (c) High-resolution N 1s XPS spectra of Ni@NC/PEI-XC after ADT (denoted as Ni@NC/PEI-XC-aging) (d) High-resolution N 1s XPS spectra of Ni/XC after 2000 cycles of ADT (denoted as Ni/XC-aging).

current density at η = 50 mV, for example, after the ADT test, Ni@NC/PEI-XC shows a mitigated degradation, retaining 67% of the activity. For comparison, the HOR activity of Ni/PEI-XC is at 58% the original density, while Ni/XC activity dramatically reduced by more than 60% after 6000 cycles (Figure 4b). The improved stability of Ni@NC/PEI-XC is also confirmed by the anodic oxidation peak at around 0.2 V in the CV profiles, related to the OH$^-$ oxidative adsorption. As shown in Figure S14, the anodic peak is more positive for Ni@NC/PEI-XC than that for Ni/XC, indicating the improved antioxidation ability and thus better stability for the carbon-layered enveloped catalyst. Further, XPS analysis of the catalyst after 2000 cycles of ADT was conducted. As shown in Figure 4c,d, most Ni^o was retained in Ni@NC/PEI-XC, while only 11.4% of Ni^o was left in Ni/XC after the aging test. This provides clear evidence that the N-doped carbon shell effectively protects the surface Ni^0 against oxidation during the electrochemical process. The corresponding XRD (Figure S15) and (HR)TEM (Figure S16) images after the aging test confirmed the morphology and phase structure of Ni@NC/PEI-XC remained, demonstrating the robustness of the Ni@NC/PEI-XC catalyst.

To understand the superior activity of Ni@NC/PEI-XC catalyst, density functional theory (DFT) calculations were performed. A set of confined models with overlayers (graphene

and N-doped graphene), as well as the pristine Ni (111) surface, were structured to study the HOR activity trend, namely, Ni-Gr, Ni-NGr (graphitic N), Ni-NGr-1 (pyridinic N), Ni-NGr-2 (pyrrolic N), and Ni (111). The optimized lattice constant of graphene and Ni is 2.46 and 3.524 Å, which is consistent with experimental values.[42,43] For Ni-Gr, Ni-NGr, and Ni-NGr-1, a (5 × 3) Ni (111) supercell with (5 × 3) graphene overlayer was used for calculations. For Ni-NGr-2, a (5 × 5) Ni (111) supercell with (5 × 5) graphene overlayer was used for calculations. For Ni, a (5 × 3) Ni (111) supercell was used for calculations. The Monkhorst−Pack k-point of 2 × 2 × 1 was used for Ni-NGr-2, and a Monkhorst−Pack k-point of 2 × 4 × 1 was used for all the other structures. All the theoretical structures are shown in Figure S17. The calculated adsorption energies of all intermediates on all surface models are listed in Table S4. We have considered two major reaction paths (see Theoretical calculations part in Supporting Information for details), and the $G_{ad}H^*$ and $G_{ad}H_2O^*$ were chosen as two independent descriptors. Therefore, the adsorption energies of OH* could be correlated with those of H* and H_2O^* (Figure 5a), in the format of $G_{ad}OH^*$ = 3.02 ×
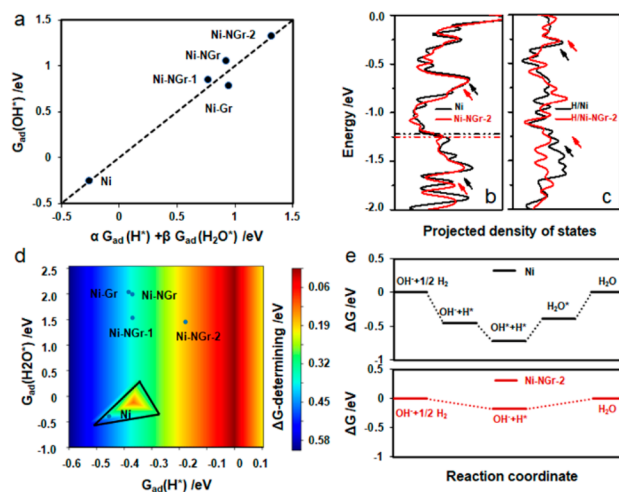
Figure 5. (a) The scaling relations for adsorption energies. (b) The projected d-band states of Ni atoms of Ni and Ni-NGr-2. (c) The projected sp-states of H atom of H/Ni and H/Ni-NGr-2. (d) Two-dimensional reaction phase diagram displaying an activity map for HOR. (e) Free energy diagrams of HOR on Ni and Ni-NGr-2.

$G_{ad}H^*$ + 0.40 × $G_{ad}H_2O^*$ + 1.28 (R^2 = 0.96). To further investigate the effect of N-doped graphene overlayer, the projected density of states (PDOS) was calculated for Ni-NGr-2 and Ni (Figure 5b,c). We found a downshift (−1.23 eV to −1.25 eV) of the d-band center of Ni atoms of the Ni-NGr-2 interface and an upshift in sp-states of the H atom of H/Ni-NGr-2 structures, which explain the weaker adsorption energy with the addition of N-doped graphene.[44] The weakened hydrogen adsorption on Ni@NC/PEI-XC to Ni/PEI-XC has also been experimentally evidenced by H_2 adsorption isotherms measurements. As depicted in Figure S18, Ni/PEI-XC exhibits stronger adsorption than Ni@NC/PEI-XC at chemisorption dominated the low-pressure region, indicating a stronger binding energy of hydrogen on Ni/PEI-XC than Ni@NC/PEI-XC. The above results are in good accordance with the XPS spectra, in which the upshifted binding energy of Ni 2p of Ni@NC/PEI-XC suggests an interfacial electron transfer from Ni to supports. Such metal−support interaction has also

been observed on P−Rh/C, NiN$_3$/C, and other catalysts.[19,38] The decrease in electron density of Ni might cause a downshift of the d band center, which consequently weakened the HBE and OHBE. For an accurate description of the HOR activity, a two-dimensional reaction phase diagram was established (Figure 5d), as the reaction free energies (ΔG) of all elementary steps could be linearly correlated with G_{ad} H* and G_{ad} H$_2$O*.[45] The activity map shows that the adsorption energies are weakened on the confined structures, which is consistent with previous theoretical and experimental works.[44,46] The activity map contains two regions with Ni-NGr-2 exhibiting a higher HOR activity, which represents two different reaction pathways, as shown in panels a and b, respectively, of Figure S19. This is in good agreement with our experimental results showing the Ni@NC/PEI-XC outperforms the Ni/XC catalyst toward HOR. The strain on the graphene overlayer and Ni substrate is uniform (0.64% and −0.64%, respectively) because of lattice mismatch. This strain will change slightly the absolute adsorption energy (ΔE_{ad}H* = 0.01 eV; ΔE_{ad}OH* = 0.03 eV; ΔE_{ad}H$_2$O* = 0.01 eV), while the relative energy variation is still valid to understand the confined effect of the N-doped graphene overlayer. Furthermore, the free energy diagram (Figure 5e) shows the optimal pathway of HOR on Ni and Ni-NGr-2, derived from reaction phase diagram analysis. A bifunctional mechanism is considered for Ni/XC, since two intermediate OH* and H* are involved in the reaction pathways. However, HBE is dominant on Ni@NC/PEI-XC because of the much weaker OH adsorption. It is interesting to note that the ΔG-determining steps are different for Ni and Ni-NGr-2. The ΔG-determining step for Ni is H$_2$O* → H$_2$O + *, while the ΔG-determining step for Ni-NGr-2 is H* + OH$^-$ → H$_2$O + * + e$^-$. Further, the ΔG of the ΔG-determining step on Ni-NGr-2 is just 0.18 eV, which is much smaller than that on Ni (0.39 eV). This result suggests the enhanced performance of Ni@NC/PEI-XC is mainly delivered from the modulated electronic structure by confinement of N doped carbon layer, which effectively optimized the adsorption of H$_{ad}$ and OH$_{ad}$ and led to small limiting energy during the HOR process.

In summary, we synthesized ultrathin layered N-doped carbon encapsulated ultrafine nickel nanoparticles as small as 3.7 nm (Ni@NC/PEI-XC). The unique core−shell architecture of the Ni@NC/PEI-XC catalyst endows it an extraordinary intrinsic activity toward HOR in alkaline electrolyte, with a high current density of 24.4 A g$^{-1}_{Ni}$ at the overpotential of 50 mV and a large exchange current density of 38 μA cm$^{-2}_{Ni}$. Most of all, Ni@NC/PEI-XC presents good stability for the HOR in the 6000 cycles of the ADT test. Combining both the experimental results and theoretical calculations, the remarkable activity and stability of Ni@NC/PEI-XC are attributed to both the abundant active sites in the ultrafine Ni particles and the advantageously modulated electronic structure in the unique core−shell structure. This work not only provides an effective strategy to design highly active and stable NPGM anodic electrocatalysts for AEMFCs but also sheds light on the underlying structure−activity relationship of HOR electrocatalysts.

■ ASSOCIATED CONTENT

Ⓢ Supporting Information

The Supporting Information is available free of charge at https://pubs.acs.org/doi/10.1021/acscatal.1c01284.

Experimental sections, supplementary tables and figures, including Tables S1−S4, Figures S1−S19 (PDF)

■ AUTHOR INFORMATION

Corresponding Authors

Jing Liu − *Electrocatalysis & Nanomaterial Laboratory, College of Materials Science & Engineering, Qingdao University of Science & Technology, Qingdao 266042, P.R. China;* Email: liuj955@qust.edu.cn

Jianping Xiao − *Dalian Institute of Chemical Physics, Chinese Academy of Sciences, Dalian 116023, P.R. China;* ⓘ orcid.org/0000-0003-1779-6140; Email: xiao@dicp.ac.cn

Luhua Jiang − *Electrocatalysis & Nanomaterial Laboratory, College of Materials Science & Engineering, Qingdao University of Science & Technology, Qingdao 266042, P.R. China;* ⓘ orcid.org/0000-0002-1462-3693; Email: luhuajiang@qust.edu.cn

Authors

Jie Wang − *Electrocatalysis & Nanomaterial Laboratory, College of Materials Science & Engineering, Qingdao University of Science & Technology, Qingdao 266042, P.R. China*

Xue Dong − *Dalian Institute of Chemical Physics, Chinese Academy of Sciences, Dalian 116023, P.R. China*

Wenzhen Li − *Department of Chemical & Biological Engineering, Iowa State University, Ames, Iowa 50011-1098, United States;* ⓘ orcid.org/0000-0002-1020-5187

Luke T. Roling − *Department of Chemical & Biological Engineering, Iowa State University, Ames, Iowa 50011-1098, United States;* ⓘ orcid.org/0000-0001-9742-2573

Complete contact information is available at:
https://pubs.acs.org/10.1021/acscatal.1c01284

Author Contributions

∥(J.W., X.D.) These authors contributed equally to this work. All authors have given approval to the final version of the manuscript.

Notes

The authors declare no competing financial interest.

■ REFERENCES

(1) Ramaswamy, N.; Mukerjee, S. Alkaline Anion-Exchange Membrane Fuel Cells: Challenges in Electrocatalysis and Interfacial Charge Transfer. *Chem. Rev.* **2019**, *119*, 11945−11979.

(2) Gottesfeld, S.; Dekel, D. R.; Page, M.; Bae, C.; Yan, Y. S.; Zelenay, P.; Kim, Y. S. Anion Exchange Membrane Fuel Cells: Current Status and Remaining Challenges. *J. Power Sources* **2018**, *375*, 170−184.

(3) Varcoe, J. R.; Atanassov, P.; Dekel, D. R.; Herring, A. M.; Hickner, M. A.; Kohl, P. A.; Kucernak, A. R.; Mustain, W. E.;

Nijmeijer, K.; Scott, K.; Xu, T.; Zhuang, L. Anion-Exchange Membranes in Electrochemical Energy Systems. *Energy Environ. Sci.* **2014**, *7*, 3135−3191.

(4) Setzler, B. P.; Zhuang, Z.; Wittkopf, J. A.; Yan, Y. Activity Targets for Nanostructured Platinum-Group-Metal-Free Catalysts in Hydroxide Exchange Membrane Fuel Cells. *Nat. Nanotechnol.* **2016**, *11*, 1020−1025.

(5) Mustain, W. E.; Chatenet, M.; Page, M.; Kim, Y. S. Durability Challenges of Anion Exchange Membrane Fuel Cells. *Energy Environ. Sci.* **2020**, *13*, 2805−2838.

(6) Sheng, W.; Gasteiger, H. A.; Shao-Horn, Y. Hydrogen Oxidation and Evolution Reaction Kinetics on Platinum: Acid vs Alkaline Electrolytes. *J. Electrochem. Soc.* **2010**, *157*, B1529−B1536.

(7) Davydova, E. S.; Mukerjee, S.; Jaouen, F.; Dekel, D. R. Electrocatalysts for Hydrogen Oxidation Reaction in Alkaline Electrolytes. *ACS Catal.* **2018**, *8*, 6665−6690.

(8) Briega-Martos, V.; Ferre-Vilaplana, A.; Herrero, E.; Feliu, J. M. Why the Activity of the Hydrogen Oxidation Reaction on Platinum Decreases as pH Increases. *Electrochim. Acta* **2020**, *354*, 136620.

(9) Cong, Y. Y.; Yi, B. L.; Song, Y. J. Hydrogen Oxidation Reaction in Alkaline Media: From Mechanism to Recent Electrocatalysts. *Nano Energy* **2018**, *44*, 288−303.

(10) An, L.; Zhao, X.; Zhao, T.; Wang, D. Atomic-Level Insight into Reasonable Design of Metal-Based Catalysts for Hydrogen Oxidation in Alkaline Electrolytes. *Energy Environ. Sci.* **2021**, *14*, 2620.

(11) Zhao, T.; Hu, Y.; Gong, M.; Lin, R.; Deng, S.; Lu, Y.; Liu, X.; Chen, Y.; Shen, T.; Hu, Y.; Han, L.; Xin, H.; Chen, S.; Wang, D. Electronic Structure and Oxophilicity Optimization of Monolayer Pt for Efficient Electrocatalysis. *Nano Energy* **2020**, *74*, 104877.

(12) Strmcnik, D.; Uchimura, M.; Wang, C.; Subbaraman, R.; Danilovic, N.; van der Vliet, D.; Paulikas, A. P.; Stamenkovic, V. R.; Markovic, N. M. Improving the Hydrogen Oxidation Reaction Rate by Promotion of Hydroxyl Adsorption. *Nat. Chem.* **2013**, *5*, 300−306.

(13) Qiu, Y.; Xin, L.; Li, Y.; McCrum, I. T.; Guo, F.; Ma, T.; Ren, Y.; Liu, Q.; Zhou, L.; Gu, S.; Janik, M. J.; Li, W. BCC-Phased PdCu Alloy as a Highly Active Electrocatalyst for Hydrogen Oxidation in Alkaline Electrolytes. *J. Am. Chem. Soc.* **2018**, *140*, 16580−16588.

(14) Durst, J.; Siebel, A.; Simon, C.; Hasche, F.; Herranz, J.; Gasteiger, H. A. New Insights into the Electrochemical Hydrogen Oxidation and Evolution Reaction Mechanism. *Energy Environ. Sci.* **2014**, *7*, 2255−2260.

(15) Sheng, W.; Zhuang, Z.; Gao, M.; Zheng, J.; Chen, J. G.; Yan, Y. Correlating Hydrogen Oxidation and Evolution Activity on Platinum at Different pH with Measured Hydrogen Binding Energy. *Nat. Commun.* **2015**, *6*, 5848.

(16) Zheng, J.; Sheng, W.; Zhuang, Z.; Xu, B.; Yan, Y. Universal Dependence of Hydrogen Oxidation and Evolution Reaction Activity of Platinum-Group Metals on pH and Hydrogen Binding Energy. *Sci. Adv.* **2016**, *2*, e1501602.

(17) Wang, Y.; Wang, G.; Li, G.; Huang, B.; Pan, J.; Liu, Q.; Han, J.; Xiao, L.; Lu, J.; Zhuang, L. Pt-Ru Catalyzed Hydrogen Oxidation in Alkaline Media: Oxophilic Effect or Electronic Effect? *Energy Environ. Sci.* **2015**, *8*, 177−181.

(18) Roy, A.; Talarposhti, M. R.; Normile, S. J.; Zenyuk, I. V.; De Andrade, V.; Artyushkova, K.; Serov, A.; Atanassov, P. Nickel-Copper Supported on a Carbon Black Hydrogen Oxidation Catalyst Integrated into an Anion-Exchange Membrane Fuel Cell. *Sustain. Sustainable Energy Fuels* **2018**, *2*, 2268−2275.

(19) Ni, W. Y.; Krammer, A.; Hsu, C. S.; Chen, H. M.; Schuler, A.; Hu, X. L. Ni₃N as an Active Hydrogen Oxidation Reaction Catalyst in Alkaline Medium. *Angew. Chem., Int. Ed.* **2019**, *58*, 7445−7449.

(20) Ni, W. Y.; Wang, T.; Schouwink, P. A.; Chuang, Y. C.; Chen, H. M.; Hu, X. L. Efficient Hydrogen Oxidation Catalyzed by Strain-Engineered Nickel Nanoparticles. *Angew. Chem., Int. Ed.* **2020**, *59*, 10797−10801.

(21) Yang, Y.; Sun, X. D.; Han, G. Q.; Liu, X.; Zhang, X. Y.; Sun, Y. F.; Zhang, M.; Cao, Z.; Sun, Y. J. Enhanced Electrocatalytic Hydrogen Oxidation on Ni/NiO/C Derived from a Nickel-Based Metal-Organic Framework. *Angew. Chem., Int. Ed.* **2019**, *58*, 10644−10649.

(22) Deng, S.; Liu, X.; Guo, X.; Zhao, T.; Lu, Y.; Cheng, J.; Chen, K.; Shen, T.; Zhu, Y.; Wang, D. Insight into the Hydrogen Oxidation Electrocatalytic Performance Enhancement on Ni Via Oxophilic Regulation of MoO₂. *J. Energy Chem.* **2021**, *54*, 202−207.

(23) Pan, Y. X.; Hu, G. H.; Lu, J. T.; Xiao, L.; Zhuang, L. Ni(OH)(2)-Ni/C for Hydrogen Oxidation Reaction in Alkaline Media. *J. Energy Chem.* **2019**, *29*, 111−115.

(24) Liu, D.; Lu, S. Q.; Xue, Y. R.; Guan, Z.; Fang, J. J.; Zhu, W.; Zhuang, Z. B. One-Pot Synthesis of IrNi@Ir Core-Shell Nanoparticles as Highly Active Hydrogen Oxidation Reaction Electrocatalyst in Alkaline Electrolyte. *Nano Energy* **2019**, *59*, 26−32.

(25) Oshchepkov, A. G.; Bonnefont, A.; Pronkin, S. N.; Cherstiouk, O. V.; Ulhaq-Bouillet, C.; Papaefthimiou, V.; Parmon, V. N.; Savinova, E. R. Nanostructured Nickel Nanoparticles Supported on Vulcan Carbon as a Highly Active Catalyst for the Hydrogen Oxidation Reaction in Alkaline Media. *J. Power Sources* **2018**, *402*, 447−452.

(26) Gao, L.; Wang, Y.; Li, H.; Li, Q.; Ta, N.; Zhuang, L.; Fu, Q.; Bao, X. A Nickel Nanocatalyst Within a h-BN Shell for Enhanced Hydrogen Oxidation Reactions. *Chem. Sci.* **2017**, *8*, 5728−5734.

(27) Yang, F. L.; Bao, X.; Zhao, Y. M.; Wang, X. W.; Cheng, G. Z.; Luo, W. Enhanced HOR Catalytic Activity of PGM-Free Catalysts in Alkaline Media: the Electronic Effect Induced by Different Heteroatom Doped Carbon Supports. *J. Mater. Chem. A* **2019**, *7*, 10936−10941.

(28) Zhou, Y.; Xie, Z.; Jiang, J.; Wang, J.; Song, X.; He, Q.; Ding, W.; Wei, Z. Lattice-Confined Ru Clusters with High CO Tolerance and Activity for the Hydrogen Oxidation Reaction. *Nat. Catal.* **2020**, *3*, 454−462.

(29) Zhuang, Z.; Giles, S. A.; Zheng, J.; Jenness, G. R.; Caratzoulas, S.; Vlachos, D. G.; Yan, Y. Nickel Supported on Nitrogen-Doped Carbon Nano-Tubes as Hydrogen Oxidation Reaction Catalyst in Alkaline Electrolyte. *Nat. Commun.* **2016**, *7*, 10141.

(30) Giles, S. A.; Yan, Y. S.; Vlachos, D. G. Effect of Substitutionally Doped Graphene on the Activity of Metal Nanoparticle Catalysts for the Hydrogen Oxidation Reaction. *ACS Catal.* **2019**, *9*, 1129−1139.

(31) Gao, Y.; Peng, H.; Wang, Y.; Wang, G.; Xiao, L.; Lu, J.; Zhuang, L. Improving the Antioxidation Capability of the Ni Catalyst by Carbon Shell Coating for Alkaline Hydrogen Oxidation Reaction. *ACS Appl. Mater. Interfaces* **2020**, *12*, 31575−31581.

(32) Chen, X.; Yu, L.; Wang, S.; Deng, D.; Bao, X. Highly Active and Stable Single Irion Site Confined in Graphene Nanosheets for Oxygen Reduction Reaction. *Nano Energy* **2017**, *32*, 353−358.

(33) Deng, J.; Ren, P.; Deng, D.; Bao, X. Enhanced Electron Penetration through an Ultrathin Graphene Layer for Highly Efficient Catalysis of the Hydrogen Evolution Reaction. *Angew. Chem., Int. Ed.* **2015**, *54*, 2100−2104.

(34) Jiang, L.; Sun, G.; Zhou, Z.; Sun, S.; Wang, Q.; Yan, S.; Li, H.; Tian, J.; Guo, J.; Zhou, B.; Xin, Q. Size-Controllable Synthesis of Monodispersed SnO2 Nanoparticles and Application in Electro-catalysts. *J. Phys. Chem. B* **2005**, *109*, 8774−8778.

(35) Lei, C.; Han, F.; Li, D.; Li, W.-C.; Sun, Q.; Zhang, X.-Q.; Lu, A. H. Dopamine as the Coating Agent and Carbon Precursor for the Fabrication of N-doped Carbon Coated Fe3O4 Composites as Superior Lithium-Ion Anodes. *Nanoscale* **2013**, *5*, 1168−1175.

(36) Liang, L.; Chen, G.; Guo, C.-Y. Enhanced Thermoelectric Performance by Self-assembled Layered Morphology of Polypyrrole Nanowire/Single-walled Carbon Nanotube Composites. *Compos. Sci. Technol.* **2016**, *129*, 130−136.

(37) Kim, S.; Choi, Y. E.; Yun, Y. S. Ruthenium Recovery from Acetic Acid Industrial Effluent Using Chemically Stable and High-Performance Polyethylenimine-coated Polysulfone-Escherichia coli Biomass Composite Fibers. *J. Hazard. Mater.* **2016**, *313*, 29−36.

(38) Su, L.; Zhao, Y.; Yang, F.; Wu, T.; Cheng, G.; Luo, W. Ultrafine Phosphorus-Doped Rhodium for Enhanced Hydrogen Electro-catalysis in Alkaline Electrolytes. *J. Mater. Chem. A* **2020**, *8*, 11923−11927.

(39) Yang, F.; Bao, X.; Li, P.; Wang, X.; Cheng, G.; Chen, S.; Luo, W. Boosting Hydrogen Oxidation Activity of Ni in Alkaline Media

through Oxygen-Vacancy-Rich CeO_2/Ni Heterostructures. *Angew. Chem., Int. Ed.* **2019**, *58*, 14179−14183.

(40) Oshchepkov, A. G.; Braesch, G.; Bonnefont, A.; Savinova, E. R.; Chatenet, M. Recent Advances in the Understanding of Nickel-Based Catalysts for the Oxidation of Hydrogen-Containing Fuels in Alkaline Media. *ACS Catal.* **2020**, *10*, 7043−7068.

(41) Kabir, S.; Lemire, K.; Artyushkova, K.; Roy, A.; Odgaard, M.; Schlueter, D.; Oshchepkov, A.; Bonnefont, A.; Savinova, E.; Sabarirajan, D. C.; Mandal, P.; Crumlin, E. J.; Zenyuk, I. V.; Atanassov, P.; Serov, A. Platinum group metal-free NiMo hydrogen oxidation catalysts: high performance and durability in alkaline exchange membrane fuel cells. *J. Mater. Chem. A* **2017**, *5*, 24433−24443.

(42) Carlsson, J. M.; Scheffler, M. Structural, Electronic, and Chemical Properties of Nanoporous Carbon. *Phys. Rev. Lett.* **2006**, *96*, 46806.

(43) Xu, L. L.; Wen, H.; Jin, X.; Bing, Q.-M.; Liu, J.-Y. DFT Study on Dry Reforming of Methane over Ni2Fe Overlayer of Ni (1 1 1) Surface. *Appl. Surf. Sci.* **2018**, *443*, 515−524.

(44) Li, H.; Xiao, J.; Fu, Q.; Bao, X. Confined Catalysis Under Two-Dimensional Materials. *Proc. Natl. Acad. Sci. U. S. A.* **2017**, *114*, 5930−5934.

(45) Guo, C.; Fu, X.; Long, J.; Li, H.; Qin, G.; Cao, A.; Jing, H.; Xiao, J. Toward Computational Design of Chemical Reactions with Reaction Phase Diagram. *Wiley Interdiscip. Rev.: Comput. Mol. Sci.* **2021**, DOI: 10.1002/wcms.1514.

(46) Li, H.; Guo, C.; Fu, Q.; Xiao, J. Toward Fundamentals of Confined Electrocatalysis in Nanoscale Reactors. *J. Phys. Chem. Lett.* **2019**, *10*, 533−539.